Macromolecules

pubs.acs.org/Macromolecules Article

Crown Ether- and Benzoxazine-Linked Porous Organic Polymers Displaying Enhanced Metal Ion and CO_2 Capture through Solid-State Chemical Transformation

Mohamed Gamal Mohamed, Wan-Chun Chang, and Shiao-Wei Kuo*

Cite This: *Macromolecules* 2022, 55, 7879−7892 Read Online

ACCESS | Metrics & More | Article Recommendations | Supporting Information

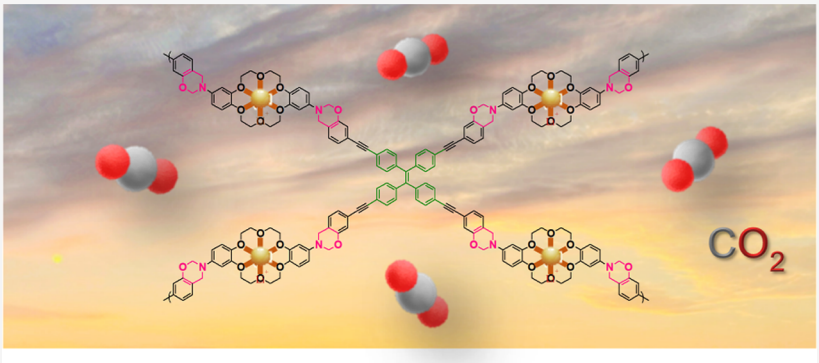

ABSTRACT: In this paper, we describe dual crown ether (CE)- and benzoxazine (BZ)-linked porous organic polymers (CE-BZ-POPs) incorporating pyrene (Py) and tetraphenylethylene (TPE) units, synthesized through a multistep process involving Schiff-base formation, reduction, Mannich condensation, and Sonogashira−Hagihara coupling, with their structures confirmed using Fourier transform infrared and solid-state nuclear magnetic resonance spectroscopy. The presence of both CE and BZ units in POPs has never been explored previously. Here, the BZ units underwent solid-state chemical transformations through thermal ring-opening polymerization without a thermal curing agent or any catalyst. The resulting Mannich bridges and phenolic units facilitated CO_2 capture, mediated through strong acid/base and/or intermolecular hydrogen bonding interactions; furthermore, the CE units bound strongly with metal ions through specific metal−ligand interactions, suggesting that these CE-BZ-POPs might be useful for wastewater treatment.

Downloaded via NATL SUN YAT-SEN UNIV on November 15, 2022 at 12:14:42 (UTC).
See https://pubs.acs.org/sharingguidelines for options on how to legitimately share published articles.

■ INTRODUCTION

Porous organic polymers (POPs), including conjugated microporous polymers, covalent organic frameworks (COFs), hyper-cross-linked polymers, porous poly(benzoxazines) (PBZ), and covalent triazine frameworks, are emerging materials possessing ultrahigh surface areas and micro/mesoporous characteristics that have been exploited in catalysis, gas capture/separation, energy storage, H_2 evolution, and pollutant removal.[1−20] The syntheses of POPs have been performed using various organic reactions, including Suzuki coupling, Schiff-base formation, Yamamoto and Sonogashira−Hagihara couplings, Mannich condensation, and Friedel−Crafts reactions.[21−34] In addition to high surface areas and pore volumes of POPs, the chemical linkages resulting from these reactions can feature a range of functionalities (e.g., triazine, imide, imine, azine, hydrazine), leading to many potential applications.[35−40] The introduction of new chemical linkages or functionalities into POPs materials through solid-state chemical transformations has also attracted much interest recently. The imine-linked POPs have been converted in the solid state to amide or oxazole linkages, while secondary amides, amines, and quinolones have been obtained directly in the solid state from their monomers.[41−47] Furthermore, Yaghi et al. reported multistep solid-state chemical transformations of an imine-COF to cyclic carbamate- and thiocarbamate-linked COFs.[48]

Polymers incorporating benzoxazine (BZ) linkages, synthesized through Mannich condensation from primary amines, phenols, and CH_2O, can feature strong intramolecular and intermolecular hydrogen bonds after they undergo thermal ring-opening polymerization (ROP) of their BZ units and these H-bonding interactions could improve the properties of PBZ materials.[49−55] Without the need for any thermal curing

Received: June 11, 2022
Revised: July 28, 2022
Published: August 9, 2022

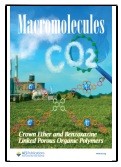

ACS Publications © 2022 American Chemical Society

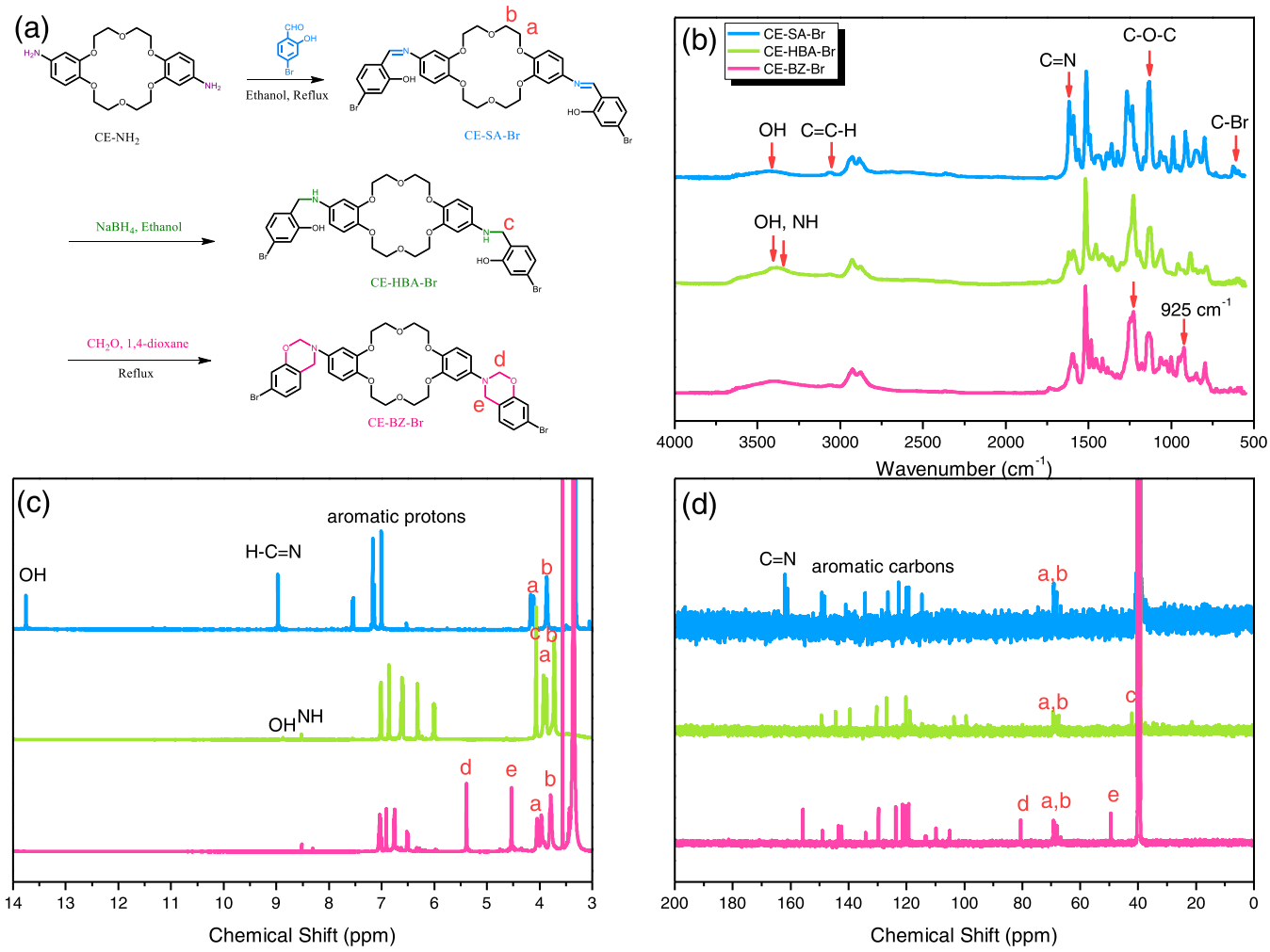

Figure 1. (a) Synthesis of CE-BZ-Br from CE-SA-Br and CE-HBA-Br. (b−d) Corresponding (b) Fourier transform infrared (FTIR), (c) ^{1}H NMR, and (d) ^{13}C NMR spectra.

agent or catalyst, the thermal ROPs of BZ rings can result in poly(benzoxazines) exhibiting low surface free energy, low dielectric constant, and high thermal stabilities.[49−55] As a result, several syntheses of BZ-linked POPs have appeared recently. For example, Xu et al. reacted a triphenol, a diamine, and CH_2O to prepare a BZ-linked POP possessing a high surface area (231 m^2 g^{-1}).[56] We also obtained a BZ-linked POP having a surface area of 72 m^2 g^{-1} through direct Mannich condensation of a triphenol, a triamine, and CH_2O.[57] Sun et al. used Sonogashira−Hagihara coupling to react a tetrahedral silicone functional monomer with two brominated BZ derivatives, obtaining BZ-linked POPs displaying high surface areas (up to 623 m^2 g^{-1}).[58] We prepared two BZ-linked POPs from the Sonogashira−Hagihara couplings of a tetrafunctionalized brominated BZ monomer with tetraethynyl-pyrene (Py-T) and tetraethynyl-tetraphenylethene (TPE-T) derivatives, with surface areas reaching as high as 325 m^2 g^{-1}.[59]

Crown ethers (CEs) are structurally simple macrocyclic host molecules that possess excellent binding ability toward organic and inorganic cations because of the electron-rich cavities.[60−64] The strengths of the supramolecular complexes formed between CEs and metal ions are dependent on the diameter of the metal ion and the size of the CE ring; accordingly, CEs have applications in biological systems, supramolecular chemistry, and nanomaterials.[60−64] Indeed, various CE-functionalized polymers have been used to extract alkali metal ions from solution in wastewater treatment.[65] For example, in a previous study, we obtained a CE-functionalized BZ monomer through Schiff-base formation from dibenzo[18]crown-6 diamine and salicylaldehyde, reduction, and Mannich condensation with CH_2O; this material exhibited excellent Li^+ ion capture ability.[54] CE-functionalized POPs have also been prepared through Friedel−Crafts and Schiff-base reactions to form imine, hydrazone, and β-ketoenamine linkages.[66−68] To the best of our knowledge, however, the combination of both CE and BZ linkages in POPs (i.e., forming CE-BZ-POPs) has not been explored previously.

In the present study, we synthesized two new CE-BZ-POPs through multistep syntheses including Schiff-base formation, reduction reaction, Mannich condensation, and Sonogashira−Hagihara coupling. First, we prepared a dibrominated CE-functionalized BZ monomer [CE-BZ-Br, Figure 1a] from *trans*-di(aminobenzo)[18]crown-6 (CE-NH_2) through Schiff-base formation, reduction, and Mannich reactions. We then obtained the two new CE-BZ-POPs of CE-BZ-Py and CE-BZ-TPE through Sonogashira−Hagihara couplings of CE-BZ-Br with Py-T and TPE-T, respectively. Because TPE exhibits aggregation-induced emission (AIE) properties, TPE-based POPs have potential for use in energy storage, optoelectronic devices, gas adsorption, and perovskite solar cells.[69−72] Finally,

https://doi.org/10.1021/acs.macromol.2c01216
Macromolecules 2022, 55, 7879−7892

we subjected these CE-BZ-POPs to ROPs through simple thermal curing polymerization in the solid state, resulting in the formation of Mannich bridges and phenolic OH groups, which we expected to interact with CO_2 through strong acid/base interactions and/or intermolecular hydrogen bonds, thereby imparting the POPs with excellent CO_2 capture ability.[73−75] In addition, we expected the CE units in these CE-BZ-POPs to bind strongly with metal ions through specific metal−ligand interactions. Herein, we discuss the chemical structures, thermal polymerization behavior, metal−ligand interactions (between the $LiClO_4$ and CE units), and ionic conductivities and CO_2 capture abilities of these two CE-BZ-POPs.

■ EXPERIMENTAL SECTION

Materials. Hydrazine monohydrate, sodium borohydride ($NaBH_4$), sodium hydroxide (NaOH), catechol (98%), dimethyl sulfoxide (DMSO), absolute EtOH, *N*,*N*-dimethylacetamide (DMAc), methanol (MeOH), *N*,*N*-dimethylformamide (DMF), toluene, chlorobenzene, acetic acid (AcOH), anhydrous $MgSO_4$, bis(2-chloroethyl)ether, CH_2Cl_2, $CHCl_3$, and $LiClO_4$ were purchased from Sigma-Aldrich. Paraformaldehyde, palladium on activated carbon (Pd/C, 10 wt %), hydrochloric acid (HCl, 37%), nitric acid (HNO_3, 65%), 1,4-dioxane (DO), and acetone were purchased from Acros. CE-NH_2, Py-T, and TPE-T were synthesized using previously reported procedures [Schemes S1 and S2].[24,54,59,75]

Dibenzo-crown-ether-4-bromosalicylaldehyde (CE-SA-Br). A solution of CE-NH_2 (4.00 g, 10.3 mmol) and 4-bromosalicylaldehyde (4.14 g, 20.6 mmol) in absolute EtOH (200 mL) was heated under reflux in a 500 mL flask equipped with a reflux condenser at 80 °C for 4 h. After cooling, the yellow solid was filtered off, washed 3 times with absolute EtOH, and dried at 50 °C for 2 days under vacuum. Yield: 85%. FTIR (KBr, cm^{-1}): 3412 (OH stretching), 3057 (C═C−H), 1613 (C═N), 1142 (C−O−C), 597 (C−Br). ^1H NMR (DMSO-d_6, 25 °C, 500 MHz): δ = 13.76 (OH), 8.98 (N═CH), 7.56−7.01 (aromatic protons), 4.17−4.12 (m, 8H), 3.87 (m, 8H). ^{13}C NMR (DMSO-d_6, 25 °C, 125 MHz): δ = 161.12−114.05, 68.79, 67.82. High-resolution FT-MS (*m*/*z*): calcd for ($C_{34}H_{32}Br_2N_2O_8$), 756.43; found, 757.05 (Figure S1).

Dibenzo-crown-ether-4-bromohydroxybenzylamine (CE-HBA-Br). A mixture of CE-SA-Br (2.00 g, 2.64 mmol), $NaBH_4$ (0.400 g, 10.6 mmol), and DMAc (20 mL) was stirred in a 100 mL flask for 1 day at 25 °C. The mixture was then poured into a large amount of ice water. After filtration, the white solid was washed 3 times with water and dried. Yield: 90%. FTIR (KBr, cm^{-1}): 3406 (OH stretching), 3346 (NH stretching). ^1H NMR (DMSO-d_6, 25 °C, 500 MHz): δ = 8.85 (OH), 8.84 (NH), 7.03−5.99 (aromatic protons), 4.07−3.88 (m, 8H), 3.88−3.73 (m, 8H), 3.73 (HNC$\underline{H}_2$). ^{13}C NMR (DMSO-d_6, 25 °C, 125 MHz): δ = 148.512, 143.80, 138.75, 134.34, 129.65, 126.23, 119.59, 118.17, 114.02, 103.02, 98.83, 69.01, 68.65, 67.92, 67.12, 41.95 ($NHCH_2$). High-resolution FT-MS (*m*/*z*): calcd for ($C_{34}H_{36}Br_2N_2O_8$), 760.47; found, 761.09 (Figure S2).

CE-BZ-Br Monomer. A solution of CE-HBA-Br (2.40 g, 3.16 mmol) and CH_2O (0.190 g, 6.28 mmol) in DO/EtOH (100 mL) was heated in a 200 mL flask at 100 °C for 1 day under N_2 atmosphere. After cooling, the solvents were evaporated, and the brown residue was dissolved in EtOAc (200 mL). This solution was washed with $NaHCO_3$ (1 N). The organic phase was concentrated under reduced pressure to provide a white solid. Yield: 80%. FTIR (KBr, cm^{-1}): 2934, 2876, 1240 (asymmetric C−O−C stretching), 925 (oxazine ring). ^1H NMR (DMSO-d_6, 25 °C, 500 MHz): δ = 7.05−6.15 (aromatic protons), 5.39 (OCH_2N), 4.54 ($ArCH_2N$), 4.06−3.97 (m, 8H), 3.81−3.79 (m, 8H). ^{13}C NMR (DMSO-d_6, 25 °C, 125 MHz): δ = 154.92−04.59, 80.14 (OCH_2N), 68.88, 67.63, 49.15 ($ArCH_2N$). High-resolution FT-MS (*m*/*z*): calcd for ($C_{36}H_{36}Br_2N_2O_8$), 784.49; found, 785.09 (Figure S3).

CE-BZ-POPs. A solution of CE-BZ-Br (392 mg, 0.500 mmol), TPE-T (107 mg, 0.250 mmol) [or Py-T (150 mg, 0.250 mmol)], CuI (4.76 mg, 0.0250 mmol), PPh_3 (6.56 mg, 0.0250 mmol), and $Pd(PPh_3)_4$ (28.9 mg, 0.0250 mmol) in DMF (10 mL) and Et_3N (10 mL) was heated at 100 °C for 3 days under reflux in a Pyrex tube to afford CE-BZ-Py POP as a red powder (yield: 75%, Scheme S3) (or CE-BZ-TPE POP as a yellow powder, yield: 80%, Scheme S4).

CE-BZ-Br/$LiClO_4$ and CE-BZ-POP/$LiClO_4$ Complexes. $LiClO_4$ was dissolved in tetrahydrofuran (THF) (10 mL) at various concentrations. Each $LiClO_4$ solution was added dropwise to a solution of CE-BZ-Br (or CE-BZ-POP) in THF (10 mL). The CE-BZ-Br/$LiClO_4$ (or CE-BZ-POP/$LiClO_4$) complex was stirred for 1 day at 25 °C. The solvent was evaporated slowly at room temperature and then each complex was subjected to thermal polymerization at 100, 150, 200, and 250 °C, for 2 h each, to form a dark brown solid.

Thermal Polymerization of the CE-BZ-Br Monomer and CE-BZ-POPs. CE-BZ-Br was subjected to thermal polymerization at 100, 150, 200, and 250 °C, for 2 h each, to provide poly(CE-BZ-Br). The CE-BZ-POPs were subjected to thermal polymerization at 100, 150, 200, 250, and 300 °C, for 2 h each, to provide poly(CE-BZ-POPs).

■ RESULTS AND DISCUSSION

Synthesis of the CE-BZ-Br Monomer. In a previous study,[19,54,59,69] we found that one-pot Mannich condensation could not be used to form a BZ monomer from the CE-NH_2 monomer directly. Thus, in the present study, we synthesized CE-BZ-Br [Figure 1a] through Schiff-base formation from CE-NH_2 and 4-bromosalicylaldehyde (to give CE-SA-Br), reduction (to give CE-HBA-Br), and finally Mannich condensation with CH_2O in DO/EtOH for 24 h at 100 °C; Figure 1b presents the Fourier transform infrared (FTIR) spectrum of each compound. The FTIR spectrum of CE-SA-Br featured signals at 3420, 3068, 1618, 1135, and 629 cm^{-1}, representing the phenolic OH, C═C−H, C═N, C−O−C (from the CE moiety), and C−Br units, respectively. The FTIR spectrum of CE-HBA-Br featured OH and NH absorptions at 3405 and 3354 cm^{-1}, respectively; the signal for the C═N group at 1618 cm^{-1} had decreased significantly after the reduction. After Mannich condensation to form the CE-BZ-Br monomer, absorption bands appeared at 925 and 1231 cm^{-1}, representing the oxazine ring and C−O stretching, respectively. Figure 1c,d displays the ^1H and ^{13}C NMR spectra, respectively, of each compound, measured at room temperature. The ^1H NMR spectrum of CE-SA-Br featured signals for the phenolic OH, N═CH, aromatic, and OCH_2 protons at 13.75, 8.98, 7.55−7.00, and 4.16−3.86 ppm, respectively. After reduction, the signal for the N═CH unit at 8.98 ppm had disappeared, with the spectrum of CE-HBA-Br featuring signals for the aromatic, OH, and NH protons at 7.01−6.00, 8.84, and 8.54 ppm, respectively, in addition to a new peak at 4.06 ppm for the $NHCH_2$ unit. The spectrum of the CE-BZ-Br monomer featured signals at 4.53 ($ArCH_2N$) and 5.38 (OCH_2N) ppm in a 1:1 ratio for the oxazine ring protons; the signal for the $NHCH_2$ unit had disappeared completely, confirming its successful synthesis. The ^{13}C NMR spectrum of CE-SA-Br featured signals for the carbon nuclei of the N═CH, aromatic, and OCH_2 units at 161.94, 148.86−115.04, and 69.15−68.06 ppm, respectively. After reduction to form CE-HBA-Br, the signal for the N═CH unit at 161.94 ppm had disappeared, with a new signal for the $NHCH_2$ unit now observed at 42.18 ppm. The spectrum of CE-BZ-Br featured signals for the oxazine ring at 49.03 ($ArCH_2N$) and 80.38 (OCH_2N) ppm, but no signal for the $NHCH_2$ unit at 42.18 ppm, confirming the successful synthesis of the monomer. High-resolution mass spectrometry confirmed the purity of the

https://doi.org/10.1021/acs.macromol.2c01216
Macromolecules 2022, 55, 7879−7892

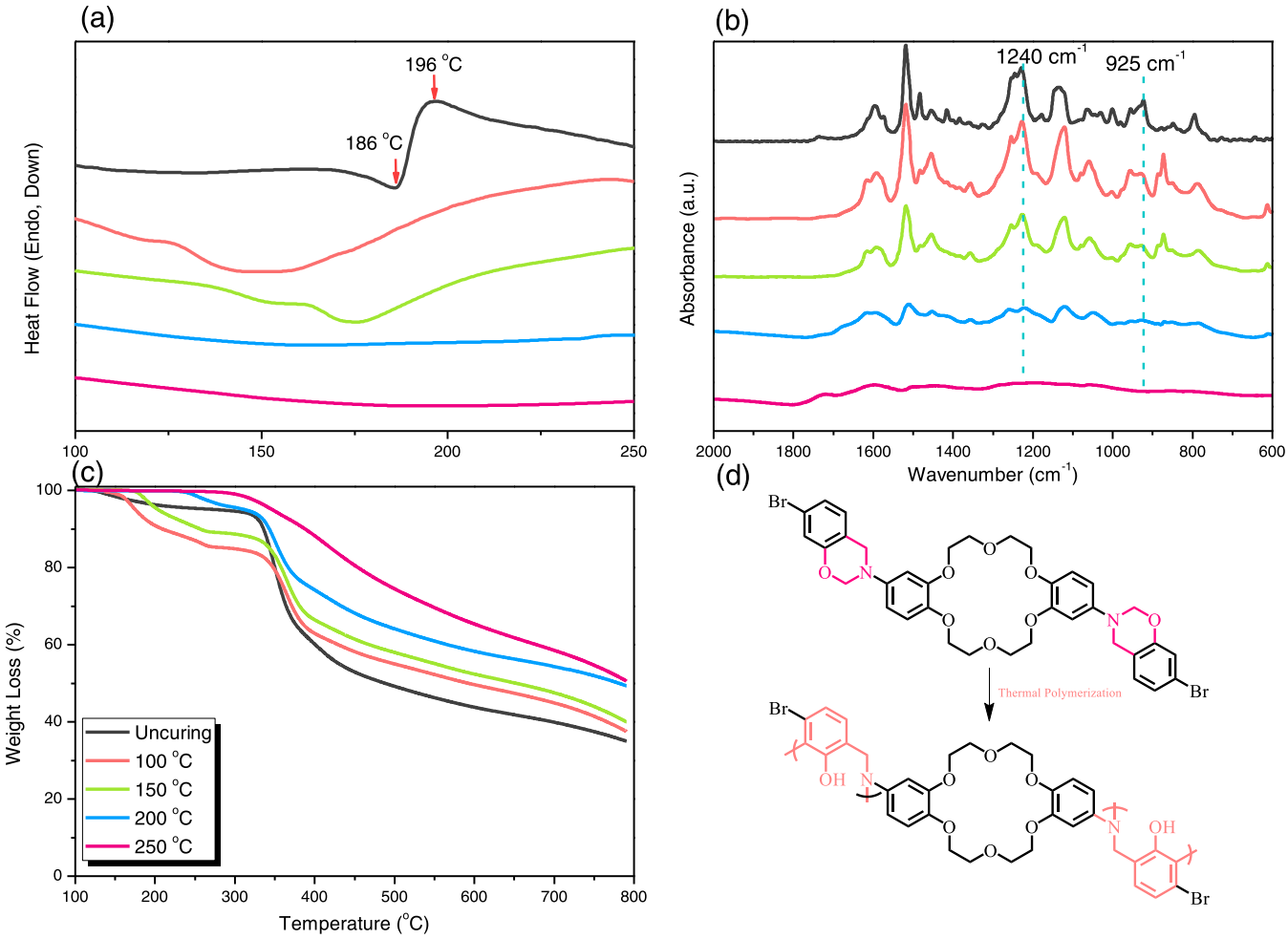

Figure 2. (a) DSC, (b) FTIR spectral, and (c) thermogravimetric analysis (TGA) analyses of the CE-BZ-Br monomer after thermal polymerization at various temperatures. (d) Schematic representation of the chemical structural change of the CE-BZ-Br monomer after thermal ROP.

CE-BZ-Br monomer (Figure S3); its experimental molecular weight was consistent with the theoretical value. Thus, all of the characterization data confirmed the high purity of our CE-BZ-Br monomer.

Polymerization Behavior of the CE-BZ-Br Monomer. Differential scanning calorimetry (DSC) of the pure CE-BZ-Br monomer after each thermal curing polymerization procedure [Figure 2a] revealed two thermal events: a signal for an endothermic melting temperature at 186 °C (confirming the high purity of the CE-BZ-Br monomer) and a signal for exothermic thermal polymerization at 196 °C with a heat of enthalpy of 137 J g^{-1}. The maximum exotherm temperature of CE-BZ-Br was much lower than that of a typical Pa-type BZ monomer (255−263 °C) and also lower than that of the CE-BZ monomer (210 °C) without the Br atom. This lower thermal curing temperature (by ca. 14 °C, relative to that of the CE-BZ monomer) was due to the flexible CE unit catalyzing the ROP, with the electron-withdrawing Br units also affecting the electron delocalization over the benzene ring, thereby changing the electron density of the phenolic OH unit and enhancing, through a strong hydrogen donor effect, the ROP of the oxazine ring. The melting temperature was depressed upon thermal polymerization, with the exothermal peak disappearing after thermal polymerization at 200 °C for 2 h, consistent with the first heating run of the uncured sample. We also used in situ FTIR spectroscopy to qualitatively investigate the ROP behavior of the CE-BZ-Br monomer [Figure 2b].

We used the signals of the oxazine ring at 925 and 1231 cm^{-1} to monitor the ROP behavior of the CE-BZ-Br monomer. The intensities of these two peaks decreased gradually upon increasing the thermal polymerization temperature from 100 to 150 °C. Total disappearance of the signals for the oxazine ring occurred when the thermal polymerization temperature was higher than 200 °C, consistent with the DSC data. We used thermogravimetric analysis (TGA) to investigate the thermal stability of CE-BZ-Br after thermal polymerization at each temperature [Figure 2c]. The temperature for 10 wt % loss (T_{d10}) of CE-BZ-Br decreased initially upon increasing the curing temperature from 100 to 150 °C, presumably because of the loss of absorbed moisture after slightly cross-linking. After thermal polymerization at 250 °C, the value of T_{d10} increased upon increasing the thermal polymerization temperature from 334 to 395 °C; this value was also higher than that of the CE-BZ monomer without Br atoms (T_{d10} = 343 °C). In addition, the char yield increased from 35 to 51 wt % after thermal polymerization at 250 °C, suggesting evaporated volatile components and the formation of a highly cross-linked poly(CE-BZ-Br) structure, such as that displayed in Figure 2d.

Analyses of CE-BZ-Br/$LiClO_4$ Complexes. Because CE units can coordinate strongly with metal ions, they can function as excellent complexing agents for the capture of

https://doi.org/10.1021/acs.macromol.2c01216
Macromolecules 2022, 55, 7879−7892

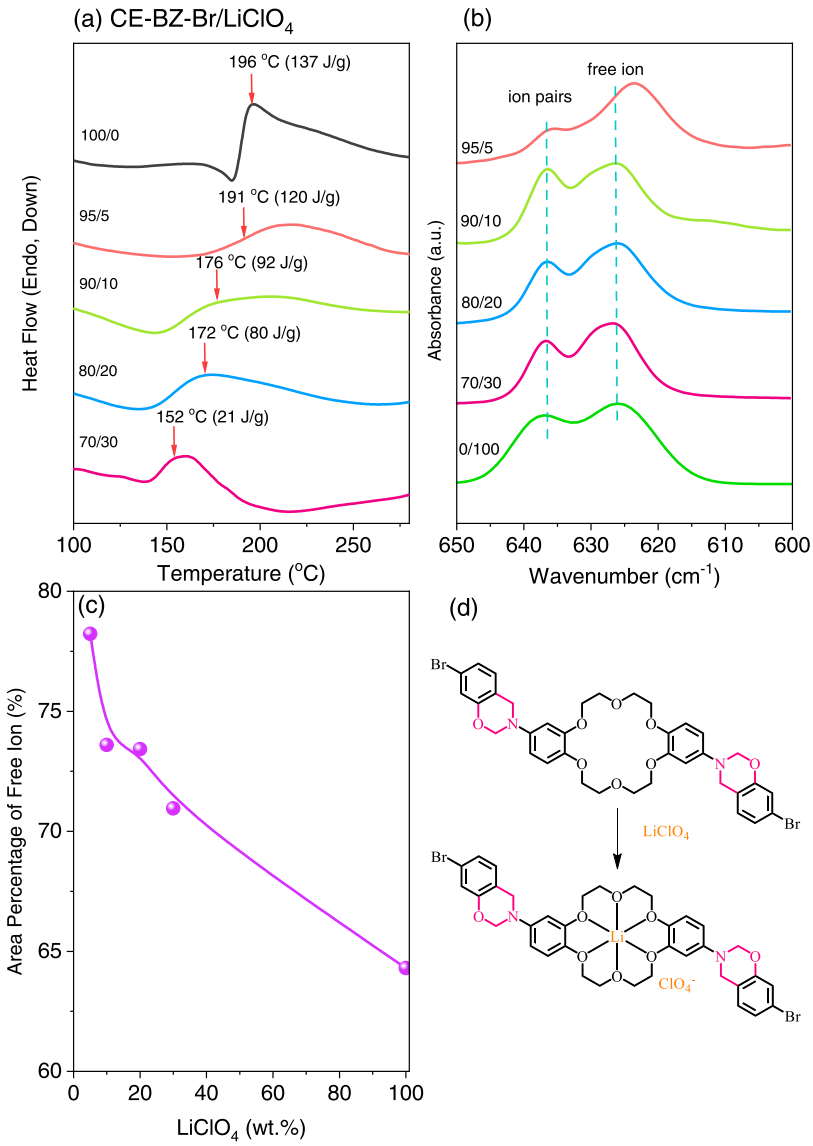

Figure 3. (a) DSC and (b) FTIR spectral analyses of various CE-BZ-Br/$LiClO_4$ complexes. (c) Area fraction of free ClO_4^- ions based on curve fitting of the results from panel (b). (d) Schematic representation of the CE-BZ-Br/$LiClO_4$ complex formed between Li^+ ions and CE units.

metal cations. In this study, we choose the lithium (Li^+) ion as the model metal cation because the ionic conductivity of Li^+ ions has been widely investigated in lithium-ion batteries and because changes in ionic conductivity can be monitored before and after the formation of Li^+/CE complexes. First, we used DSC to investigate the ROP behavior of the CE-BZ-Br/$LiClO_4$ complex [Figure 3a]; here, the thermal polymerization temperature and heat of thermal reaction both decreased upon increasing the concentration of $LiClO_4$. For example, when the $LiClO_4$ content was 30 wt %, the thermal polymerization peak appeared at 152 °C, much lower than the value of 186 °C for the CE-BZ/$LiClO_4$ = 70:30 complex system (without Br atoms). This phenomenon can be explained by considering that the CE unit, Br atom, and Li^+ ion could all act as catalysts for the ROP of the oxazine units; indeed, various metal ions (e.g., Fe^{3+}, Zn^{2+}, Cu^{2+}, and Li^+) can function as effective catalysts for the ROP of BZ monomers through metal ion coordination to the oxazine ring, metal ion electrophilic attack on the oxazine ring, and phenoxy and phenolic structural rearrangement.[76,77]

We used FTIR spectroscopy to analyze the specific CE/Li^+ ion coordination [Figure 3b]. In the spectrum for pure $LiClO_4$, a peak appeared at 637 cm^{-1} for the ion pairs formed between ClO_4^- anions and Li^+ cations, and another appeared for the free ClO_4^- ions at 626 cm^{-1}; these signals red-shifted to 636 and 623 cm^{-1}, respectively, in the presence of CE-BZ-Br, suggesting that the Li^+ cations coordinated with the CE and oxazine ring units through ion−dipole interactions. Curve fitting of these two bands into Gaussian peaks revealed that the area fraction of the free ClO_4^- ions decreased upon increasing the $LiClO_4$ concentration; thus, during ROP of the CE-BZ-Br monomer, the Li^+ ions could coordinate effectively with the CE moiety, as displayed in Figure 3d, and also with the N or O atom of the oxazine ring. Because Li^+ cations possessed catalytic behavior for ROP of the oxazine ring, we used thermal dynamic DSC analyses to examine thermal polymerization kinetics of pure CE-BZ-Br and CE-BZ-Br/$LiClO_4$ = 80:20 complexes at various heating rates [Figure 4a,b]. As expected, increasing the heating rate from 5 to 20 °C min^{-1} shifted the thermal polymerization temperature (T_p) due to the delay of

https://doi.org/10.1021/acs.macromol.2c01216
Macromolecules 2022, 55, 7879−7892

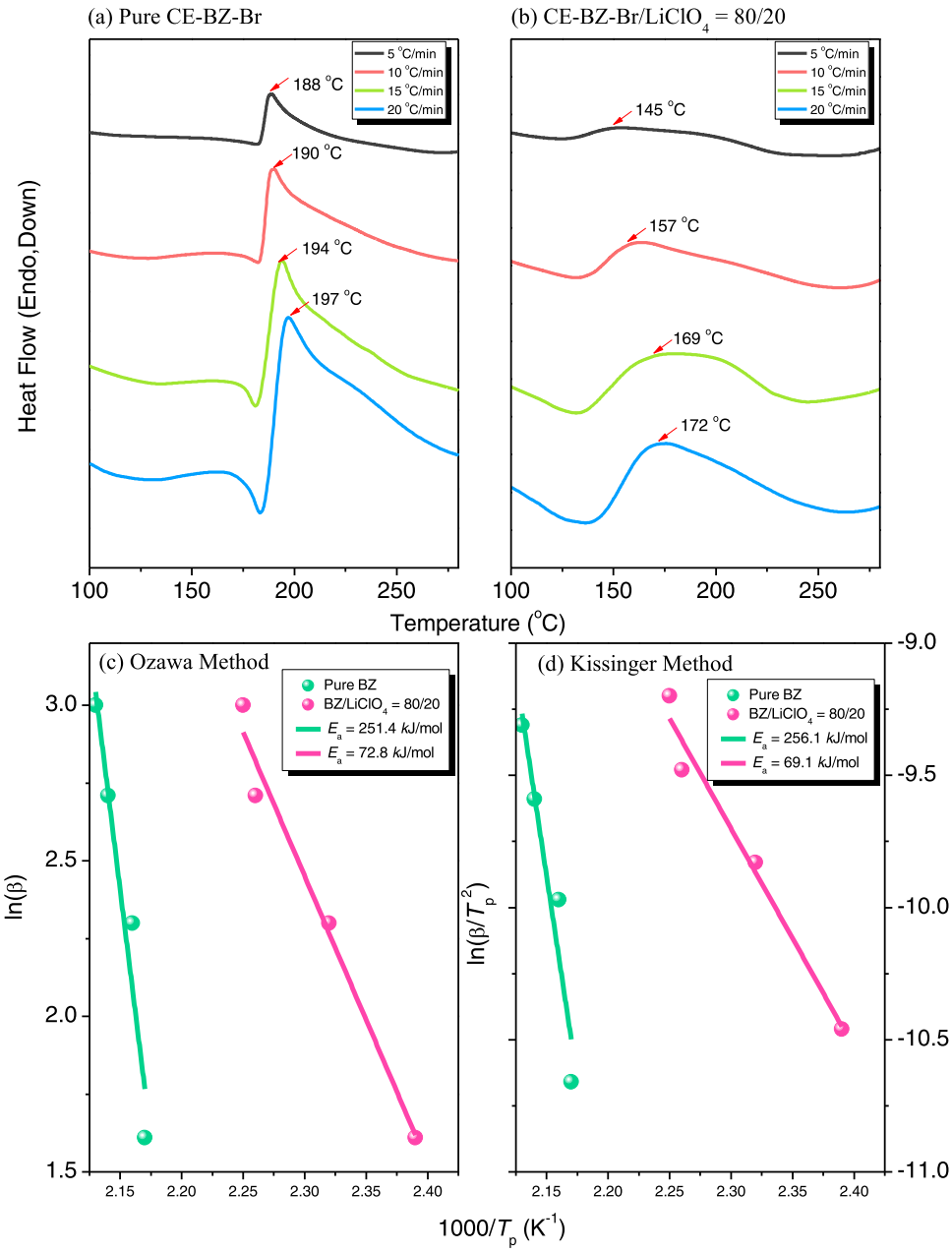

Figure 4. (a, b) DSC dynamic heating scans of the (a) pure CE-BZ-Br monomer and (b) CE-BZ-Br/$LiClO_4$ = 80:20 complex, measured at various heating rates. (c, d) Corresponding values of E_a for both systems, calculated using (c) Ozawa and (d) Kissinger methods.

the thermal polymerization reaction. We used the Ozawa and Kissinger method to measure the thermal polymerization kinetics of the BZ systems, with the activation energy (E_a) readily determined using eqs S1 and S2; Figure 4c,d summarizes the respective fitting data. The values of E_a of the CE-BZ-Br/$LiClO_4$ = 80:20 complex determined using both equations were much lower than those of the pure CE-BZ-Br, suggesting that the Li^+ ions did indeed possess catalytic behavior to accelerate the ROP of the oxazine ring. The value of E_a obtained using the Kissinger method (69.1 kJ mol^{-1}) was also lower than that of the CE-BZ/$LiClO_4$ = 80:20 complex (without Br atoms; 74.91 kJ mol^{-1}),[54] consistent with the thermal polymerization peak of CE-BZ-Br being much lower than that of CE-BZ because of coordination with $LiClO_4$.

Synthesis and Polymerization Behavior of CE-BZ-POPs. We synthesized CE-BZ-Py and CE-BZ-TPE POPs through Sonogashira−Hagihara couplings of CE-BZ-Br with Py-T and TPE-T, respectively [Schemes S3, S4, and Figure 5a].

We used DSC analyses to examine their thermal polymerization behavior and confirm the presence of BZ linkages in these two POPs [Figure 5b]. The CE-BZ-Py POP exhibited a broad exothermic thermal polymerization peak (at 259 °C) with a heat of reaction of 70 J g^{-1}; the CE-BZ-TPE POP also displayed a broad exothermic thermal polymerization peak (at 257 °C), with a heat of reaction of 38 J g^{-1}. FTIR spectra confirmed the presence of oxazine rings in these two POPs [Figure 5c], with the CE-BZ-Py (CE-BZ-TPE) POP displaying signals for acetylene units, C−O−C groups (from CE units), and oxazine rings at 2201 (2204), 1121 (1126), and 949 (953) cm^{-1}, respectively, confirming the successful incorporation of CE and BZ linkages in these two POPs. Solid-state ^{13}C NMR

https://doi.org/10.1021/acs.macromol.2c01216
Macromolecules 2022, 55, 7879−7892

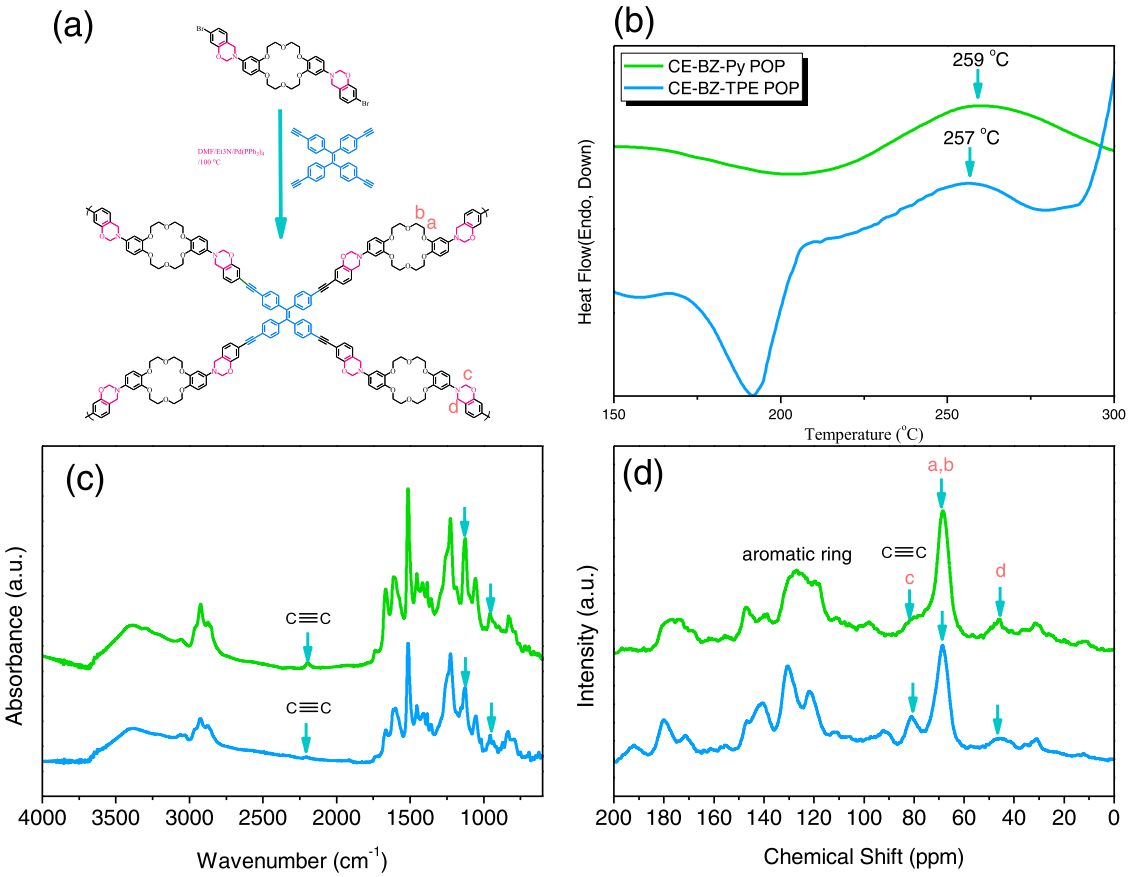

Figure 5. (a) Synthesis of the CE-BZ-TPE POP from CE-BZ-Br and TPE-T. (b−d) Corresponding (b) DSC, (c) FTIR spectral, and (d) ^{13}C solid-state NMR spectral analyses.

spectra confirmed the presence of CE and BE linkages in the POPs [Figure 5d]. The spectra of the CE-BZ-Py and CE-BZ-TPE POPs featured signals for aromatic carbon nuclei at 147.61−118.69 and 146.60−121.37 ppm, respectively, and for the OCH_2 units of the CE moieties at 68.06 and 68.73 ppm, respectively; most importantly, signals appeared at 81.81 and 88.55 ppm, respectively, for OCH_2N and internal triple bond units and at 45.26 or 46.52 ppm, respectively, for the $ArCH_2N$ units, confirming the chemical structures of these two POPs. X-ray photoelectron spectroscopy (XPS) analysis was used to describe the structures of CE-BZ-Py and CE-BZ-TPE POPs [Figure S4]. As shown in Figure S4a, the XPS profile of CE-BZ-Py POP showed strong peaks at 285.56, 396.71, and 532.65 eV, corresponding to the presence of C 1s, N 1s, and O 1s. However, the peaks of C 1s, N 1s, and O 1s in the CE-BZ-TPE POP were found at 281.76, 397.31, and 532.05 eV, respectively [Figure S4b]. Both CE-BZ-Py and CE-BZ-TPE POPs had an amorphous structure based on X-ray diffraction (XRD) analyses [Figure S5]. Elemental mapping of scanning electron microscopy (SEM) and transmission electron microscopy (TEM) confirmed the presence of C, N, and O in the CE-BZ-Py and CE-BZ-TPE POPs materials [Figures S6a−c, S7a−c, S8a, and S9a].

We measured N_2 adsorption/desorption isotherms at 77 K to determine the porosities of CE-BZ-Py and CE-BZ-TPE POPs [Figure 6a,b, respectively]. Based on the IUPAC definition, these two sorption isotherms could both be classified as type I isotherms. For both POPs, a steep and quite weak uptake of N_2 gas occurred at relative low pressure, indicating the presence of microporous structures. For the CE-BZ-Py POP, the Brunauer−Emmett−Teller (BET) specific surface area and total pore volume were 11.9 $m^2\ g^{-1}$ and 0.073 $cm^3\ g^{-1}$, respectively; for the CE-BE-TPE POP, they were 33.5 $m^2\ g^{-1}$ and 0.087 $cm^3\ g^{-1}$, respectively. Although high surface areas have been proposed for CE-based POPs,[67,68,78] our CE-BZ-POPs had low specific surface areas, presumably because the CE units had flexible structures relative to those of the other rigid building blocks used for the synthesis of POPs. This finding is consistent with those of Chi et al. and Zhao et al. who obtained specific surface areas for [18]crown-6-based POPs of 21 and 47 $m^2\ g^{-1}$, respectively.[79,80] Furthermore, the hysteresis loop of the N_2 adsorption/desorption curve of the CE-BZ-TPE POP did not completely close due to its CE moieties acting as flexible units within the POP framework, leading to elastic deformation, consistent with the low surface areas of these CE-BZ-POPs. We used nonlocal density functional theory (NLDFT) to determine the corresponding pore size distributions of these two CE-BZ-POPs [insets to Figure 6a,b]; the CE-BZ-Py POP contained micro/mesopores having sizes in the range of 1.81−3.76 nm, while the CE-BZ-TPE POP has sizes in the range of 1.76−3.35 nm. SEM images of the surface morphologies [Figure 6c,d] indicated the presence of interconnected small aggregated spherical structures for both CE-BZ-POPs, with irregular amorphous properties and microporous structures. TEM images also revealed the presence of irregular microporous structures [Figure 6e,f].

We used FTIR spectroscopy and TGA to investigate the chemical transformations of these two CE-BZ-POPs through solid-state ROP, through analyses performed before and after

https://doi.org/10.1021/acs.macromol.2c01216
Macromolecules 2022, 55, 7879−7892

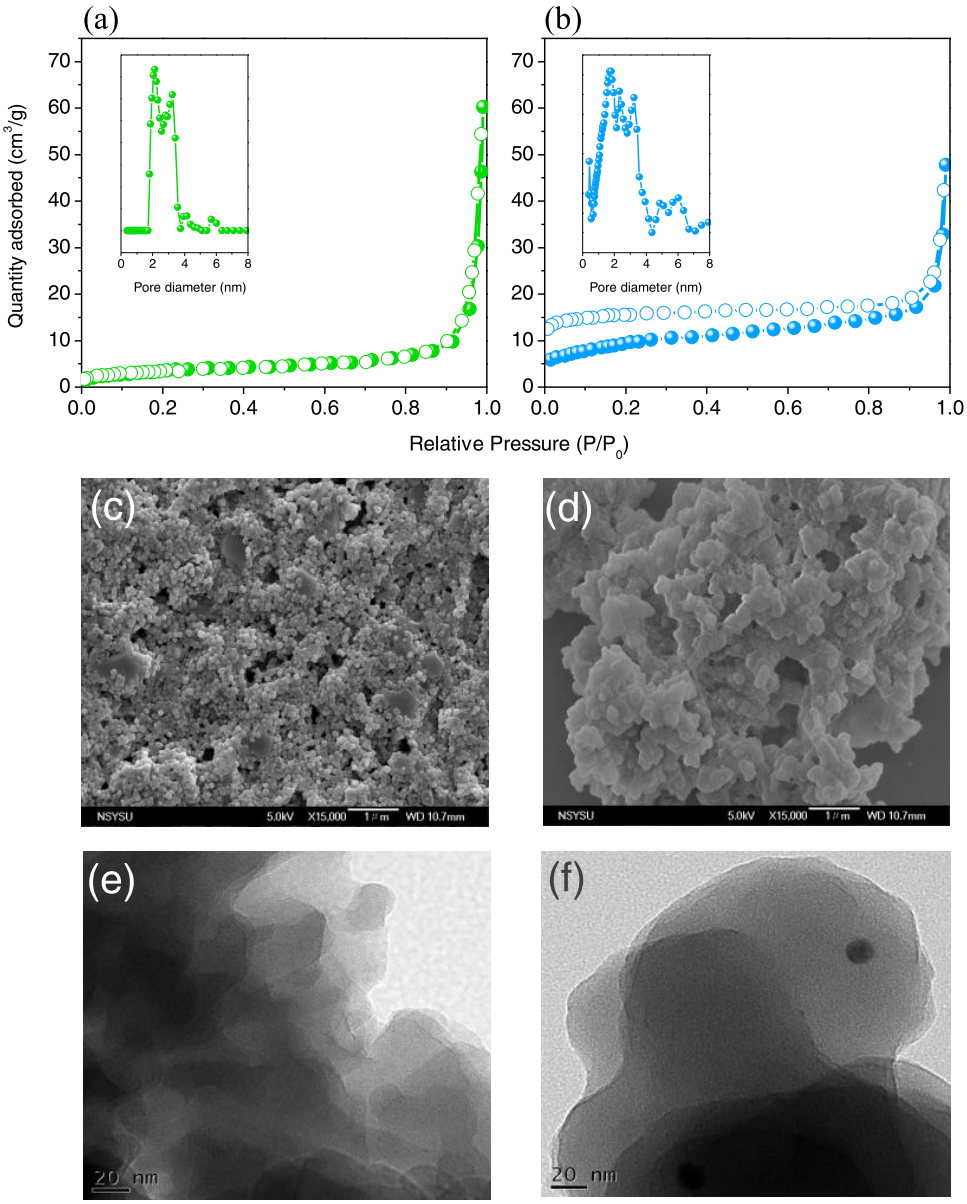

Figure 6. (a, b) N_2 adsorption/desorption isotherms, (c, d) SEM images, and (e, f) TEM images of (a, c, e) CE-BZ-Py and (b, d, f) CE-BZ-TPE POPs.

thermal polymerization [Figure 7a–d]. As displayed in Figure 7a,b, the signals for C–O stretching and the oxazine ring near 1242 and 949 cm^{-1}, respectively, disappeared completely after thermal polymerization of both the CE-BZ-Py and CE-BZ-TPE POPs at 300 °C for 2 h, consistent with the DSC data in Figure 5b. Very broad signals appeared in the range of 3600–2500 cm^{-1} after thermal ROP, indicating that large amounts of phenolic OH units formed and underwent intramolecular [OH···N] and [OH···π] and intermolecular [OH···O] interactions, as have been discussed in many previous studies.[54] In addition, the signals for internal acetylene bonds of CE-BZ-Py and CE-BZ-TPE POPs at 2204 and 2201 cm^{-1} remained after thermal polymerization at 300 °C for 2 h, indicating that the frameworks of both CE-BZ-POPs remained intact at high temperature. We used TGA to examine the thermal stabilities of these two CE-BZ-POPs [Figure 7c,d]. The value of T_{d10} and the char yield for the uncured CE-BZ-Py POP were 328 °C and 44.9 wt %, respectively; for the uncured CE-BZ-TPE POP, they were 339 °C and 48.9 wt %, respectively. After thermal polymerization, the value of T_{d10} and char yield for poly(CE-BZ-Py) both increased to 403 °C and 50.8 wt %, respectively; similarly, for poly(CE-BZ-TPE), they both increased to 421 °C and 51.8 wt %, respectively. Figure 7e,f presents SEM images of poly(CE-BZ-Py) and poly(CE-BZ-TPE), again revealing interconnected small aggregated spherical structures with large amounts of micropores; their surfaces presumably featured large amounts of phenolic OH groups, Mannich bridges, and CE units after the thermal ROP reaction, as displayed in Figure 8a. Elemental mapping of TEM revealed the presence of C, N, and O in the poly(CE-BZ-Py) and poly(CE-BZ-TPE) POPs frameworks [Figures S8b and S9b]. In addition, XPS data of poly(CE-BZ-Py) and poly(CE-BZ-TPE) POPs [Figure S10] revealed the presence of C 1s, N 1s, and O 1s in their framework. Figure 8b,c provides the CO_2 capture behavior, measured at 298 K at

https://doi.org/10.1021/acs.macromol.2c01216
Macromolecules 2022, 55, 7879–7892

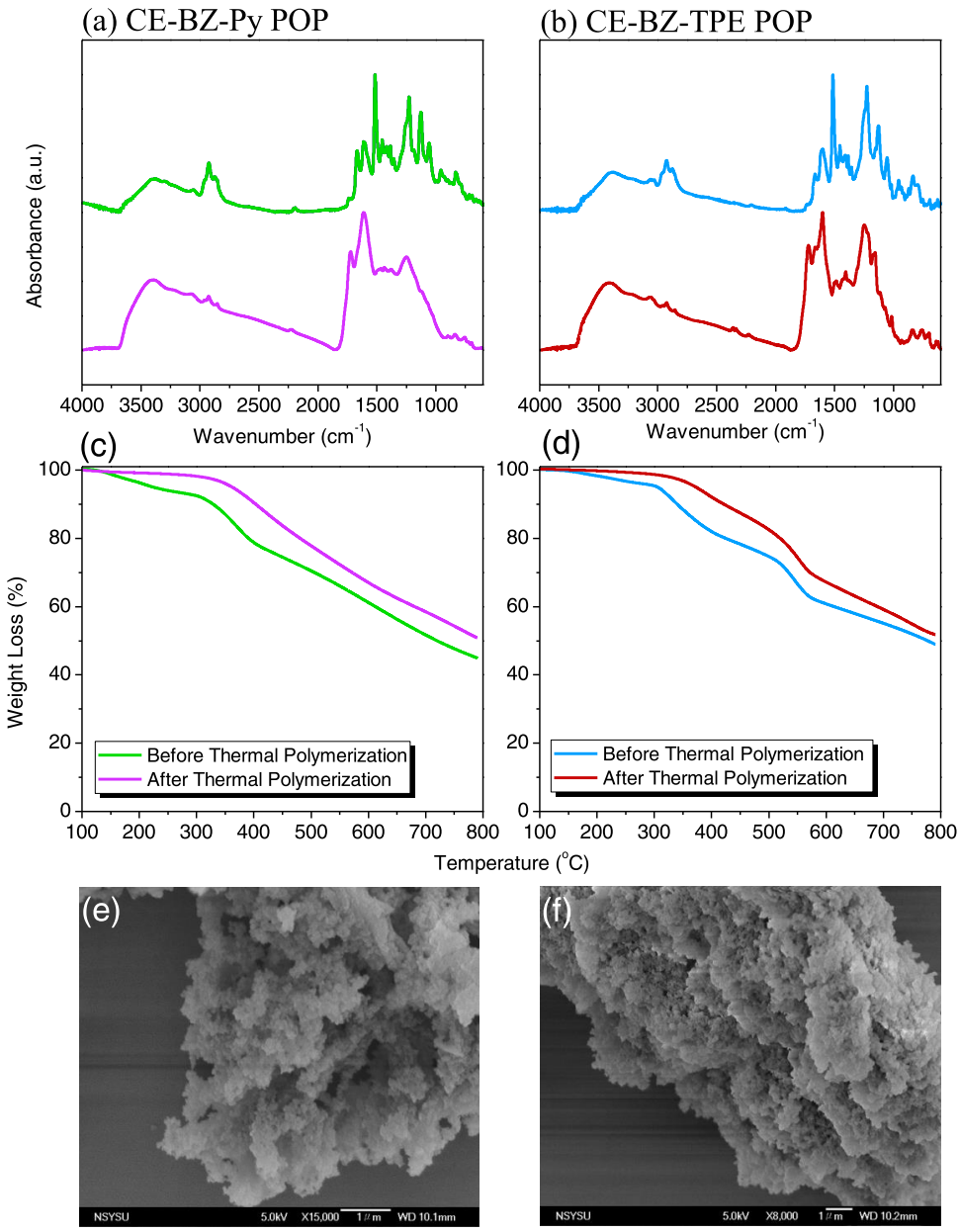

Figure 7. (a, b) FTIR spectral and (c, d) TGA analyses of (a, c) CE-BZ-Py and (b, d) CE-BZ-TPE POP, performed before and after thermal polymerization. (e, f) SEM images of (e) CE-BZ-Py and (f) CE-BZ-TPE POPs, recorded after thermal polymerization.

1 bar, of the CE-BZ-POPs before and after their thermal polymerization [Figure 8a].

CE-BZ-Py and CE-BZ-TPE POPs displayed CO_2 capacities of 0.63 (2.77 wt %) and 0.58 (2.55 wt %) mmol g^{-1}, respectively. After thermal ROP and the formation of poly(CE-BZ-Py) and poly(CE-BZ-TPE), the CO_2 capacities increased significantly to 1.72 (7.56 wt %) and 4.36 (19.18 wt %) mmol g^{-1}, respectively. The CO_2 capture abilities of both CE-BZ-TPE and poly(CE-BZ-TPE) POPs were higher than those of CE-BZ-Py and poly(CE-BZ-Py) POPs because the former featured higher surface areas and pore volumes, which favored CO_2 capture. After the thermal ROPs formed the poly(CE-BZ-Py) and poly(CE-BZ-TPE) POPs, the CO_2 uptake capacities were higher than those of the CE-BZ-Py and CE-BZ-TPE POPs, presumably because of the presence of highly abundant N atoms and phenolic OH groups in the former pair, as a result of solid-state chemical transitions in their polymeric frameworks; these new units were capable of forming acid/base and hydrogen bonding interactions that stabilized the coordination of CO_2 gas through [N···C═O] and [OH···O═C] interactions, thereby resulting in higher degrees of CO_2 capture. Furthermore, poly(Py-TPE-BZ) and poly(TPE-TPE-BZ) POPs, formed without CE units, had CO_2 uptakes of 2.20 and 2.21 mmol g^{-1}, respectively, at 298 K at 1 bar.[59] Notably, Ma et al. reported that the BZ-functionalized POPs BPOP-1 and BPOP-2 had CO_2 uptakes of 0.98 and 0.67 mmol g^{-1},[58] respectively, while Tan et al. noted that the BZ-functionalized POPs BoxPOP-1, BoxPOP-2, and BoxPOP3 displayed CO_2 uptakes of 0.91, 1.04, and 0.29 mmol g^{-1}, respectively, at 298 K at 1 bar.[56] Our poly(TPE-TPE-BZ) POPs displayed a higher CO_2 uptake value (4.36 mmol g^{-1}) than those of AT-F1-900 (4.16 mmol g^{-1}), AT-F2-900 (4.25 mmol g^{-1}), AT-F3-900 (4.04 mmol g^{-1}), AT-F2-600 (3.52 mmol g^{-1}), and AT-P2-900 (3.88 mmol g^{-1}).[81]

https://doi.org/10.1021/acs.macromol.2c01216
Macromolecules 2022, 55, 7879−7892

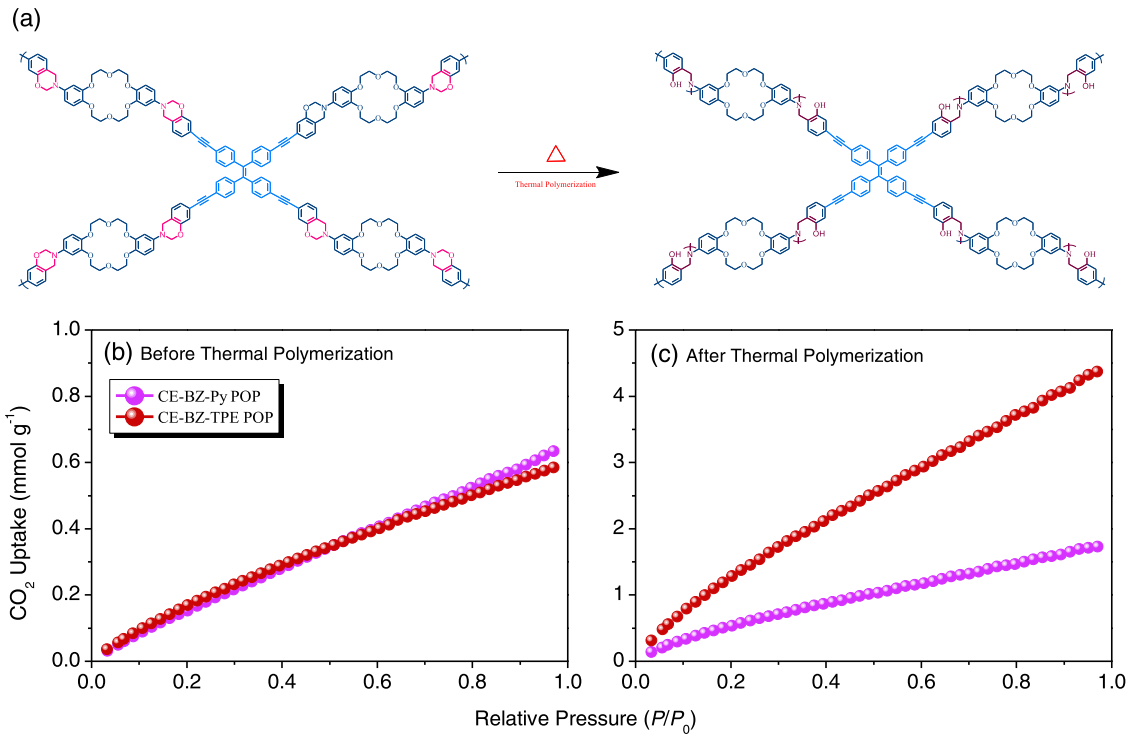

Figure 8. (a) Schematic representation of the chemical structural change of the CE-BZ-TPE POP after thermal ROP. (b, c) CO_2 uptake ability of the CE-BZ-POPs (b) before and (c) after thermal polymerization.

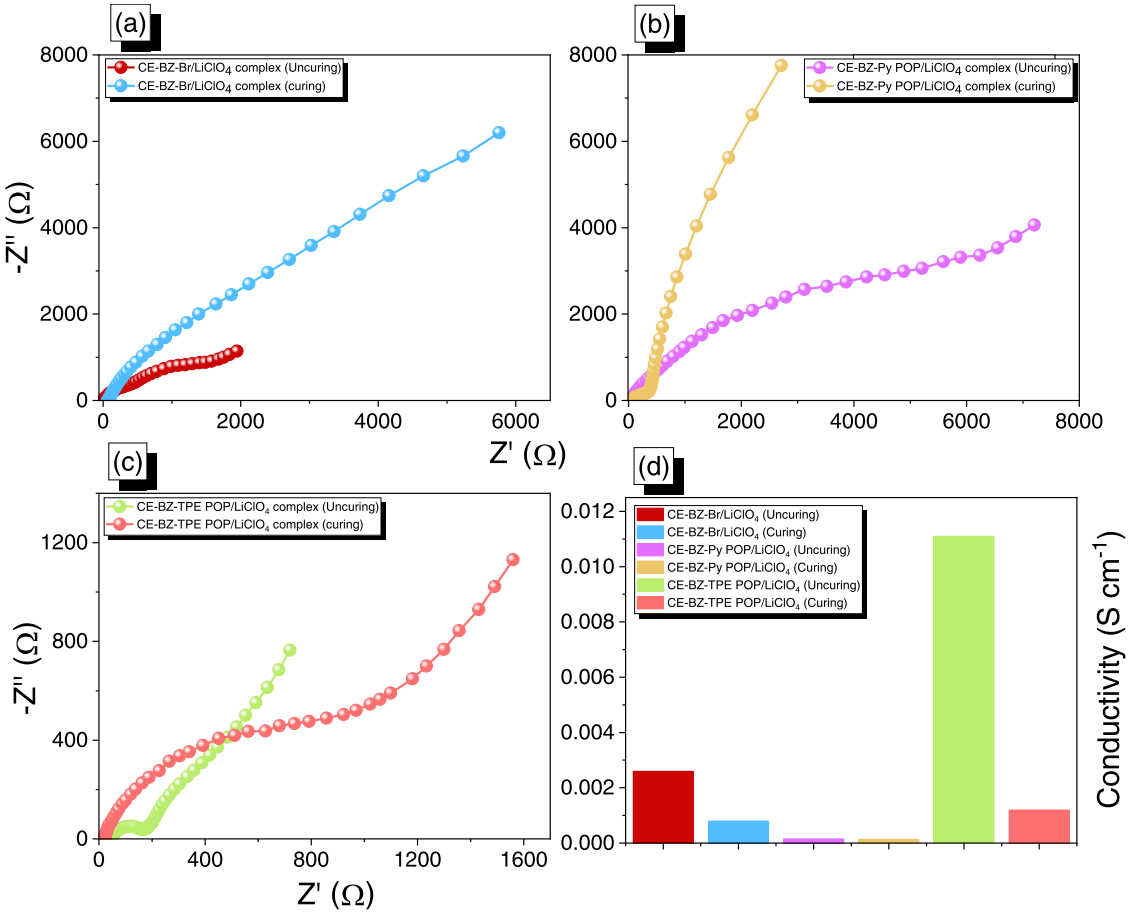

Figure 9. (a–c) EIS spectra (Nyquist plot) of (a) CE-BZ-Br/$LiClO_4$ = 80:20 complex, (b) CE-BZ-Py POP/$LiClO_4$ = 80:20 complex, and (c) CE-BZ-TPE POP/$LiClO_4$ = 80:20 complex, recorded before and after ROP. (d) Corresponding conductivities measured after EIS fitting.

https://doi.org/10.1021/acs.macromol.2c01216
Macromolecules 2022, 55, 7879−7892

Thus, our CE-functionalized BZ-linked POPs presumably also provided strong intermolecular interactions through CE··· CO_2 complexation, thereby improving the CO_2 capture ability.[82] In addition, TAPP(H2)-B18C6-POP and TAPP-(Co)-B18C6-POP, CE-functionalized POPs without BZ linkages, exhibited CO_2 uptake capacities of 0.90 and 1.15 mmol g^{-1}, respectively, at 298 K at 1 bar;[78] thus, the BZ functionalities in our CE-POPs also appeared to provide additional strong intermolecular interactions with CO_2. As a result, taking advantage of the presence of both CE and BZ units, our POPs after thermal ROP exhibited excellent CO_2 uptake capacities; indeed, they are the highest ever reported among CE- or BZ-functionalized POPs.

In a previous study,[54] we found that the chain mobility of the polymer increased upon increasing the temperature, and that the presence of Li^+ and ClO_4^+ ions led to high conductivity. Nevertheless, upon increasing the temperature, the chain mobility of the BZ-functionalized POPs decreased because the cross-linking density increased and, thus, the ionic conductivity changed after thermal ROP. Figure 9 reveals the ionic conductivities of CE-BZ-Br and CE-BZ-POP complexed with 20 wt % $LiClO_4$, confirming that the chain mobility changed during thermal ROP. In general, the ionic conductivity is dependent on the charge carrier concentration, ionic charge, and ionic mobility. We used electrochemical impedance spectroscopy (EIS) to study the effects of curing on the conductivity.

The obtained EIS data in Figure S11 were fitted with an equivalent circuit to compare the series resistance (R_s), charge transfer resistance (R_{ct}), constant phase elements representing both electric double layer capacitance (CPE-EDLC), and pseudocapacitive (CPE-P) behavior, and the Warburg element (Z_w).[83,84] We used a Randles cell to match the well-defined Warburg diffusion (W_d) combined with charge transfer (R_{ct}) and solution (R_s) resistance (Table S1). The impedances of the CE-BZ-Br, CE-BZ-Py POP, and CE-BZ-TPE POP complexes with 20 wt % $LiClO_4$ reached 2.6×10^{-3}, 1.5×10^{-4}, and 1.1×10^{-2} S cm^{-1}, respectively, prior to thermal ROP at 25 °C; after thermal ROP, they decreased significantly to 8×10^{-4}, 1.4×10^{-4}, and 1.2×10^{-3} S cm^{-1}, respectively. Prior to thermal ROP, the CE-BZ-Br/$LiClO_4$ complex possessed the highest ionic conductivity because the Li^+ ions could strongly coordinate with the CE and BZ units. The ionic conductivity of the CE-BZ-POP/$LiClO_4$ complexes was lower prior to thermal ROP because the chain mobility was restricted after Sonogashira−Hagihara coupling had formed the CE-BZ-POPs. After thermal ROP of all of the complex systems, the ionic conductivities decreased because the chain and ionic mobilities remained limited; thus, the Li^+ ions transformed back to $LiClO_4$ ion pairs, resulting in lower ionic conductivity. Most importantly, thermal ROP of the CE-BZ-POP/$LiClO_4$ complex improved its thermal and mechanical properties, compared with those of other thermoplastic polymers (e.g., poly(ethylene oxide) (PEO), poly(caprolactone) (PCL), and poly(methyl methacrylate) (PMMA)), making it a potential material for use in next-generation solid polymer electrolytes and also for metal ion capture in wastewater treatment.

■ CONCLUSIONS

We have synthesized CE-BZ-POPs, incorporating Py and TPE units through Schiff-base formation, reduction, Mannich condensation, and Sonogashira−Hagihara coupling, and examined them using DSC, TGA, FTIR spectroscopy, and solid-state NMR spectroscopy. The presence of both CE and BZ functional groups in these POPs ensured not only that solid-state chemical transformations could be performed through thermal ROP of the BZ units but also that the CE units could provide strong coordination ability with metal ions and CO_2. Because the BZ units could undergo thermal ROP in the absence of any catalyst or thermal curing agent, these POPs readily transformed to introduce Mannich bridges and phenolic units, which facilitated CO_2 capture through strong acid/base and intermolecular hydrogen bonding interactions. Therefore, taking advantage of the presence of both the CE and BZ units, our CE-BZ-POPs possessed CO_2 capture abilities higher than those of POPs, featuring only CE or BZ linkages. Accordingly, we believe that these CE-BZ-POPs could be useful materials for next-generation solid polymer electrolytes and wastewater treatment systems.

■ ASSOCIATED CONTENT

Supporting Information

The Supporting Information is available free of charge at https://pubs.acs.org/doi/10.1021/acs.macromol.2c01216.

Details about the characterization methods, values of different parameters of fitted Nyquist plots, synthesis of Py-TMS and Py-T, synthesis of TPE-TMS and TPE-T, synthesis of CE-BZ-Py POP, synthesis of CE-BZ-TPE POP, high-resolution mass spectra of CE-SA-Br, CE-HBA-Br, and CE-BZ-Br; XPS survey spectra of the as-prepared CE-BZ-Py POP and CE-BZ-TPE POP before thermal curing; XRD profiles of CE-BZ-Py POP and CE-BZ-TPE POP; SEM images, elemental mapping (EDX) profile of the as-prepared CE-BZ-Py POP, and elemental content in the CE-BZ-Py POP sample; SEM images, elemental mapping (EDX) profile of the as-prepared CE-BZ-TPE POP, and elemental content in CE-BZ-TPE POP sample; XPS survey spectra of the as-prepared poly(CE-BZ-Py) and poly(CE-BZ-TPE) POPs after polymerization; Nyquist plots and equivalent fitted circuit of the CE-BZ-Br/$LiClO_4$ = 80:20 complex, CE-BZ-Py POP/$LiClO_4$ = 80:20 complex, and CE-BZ-TPE POP/ $LiClO_4$ = 80:20 complex recorded before and after ROP and the equivalent circuit of the CE-BZ-POPs (PDF)

■ AUTHOR INFORMATION

Corresponding Author

Shiao-Wei Kuo − *Department of Materials and Optoelectronic Science, Center for Functional Polymers and Supramolecular Materials, National Sun Yat-Sen University, Kaohsiung 804, Taiwan;* orcid.org/0000-0002-4306-7171; Email: kuosw@faculty.nsysu.edu.tw

Authors

Mohamed Gamal Mohamed − *Department of Materials and Optoelectronic Science, Center for Functional Polymers and Supramolecular Materials, National Sun Yat-Sen University, Kaohsiung 804, Taiwan;* orcid.org/0000-0003-0301-8372

Wan-Chun Chang − *Department of Materials and Optoelectronic Science, Center for Functional Polymers and Supramolecular Materials, National Sun Yat-Sen University, Kaohsiung 804, Taiwan*

Complete contact information is available at:

https://doi.org/10.1021/acs.macromol.2c01216
Macromolecules 2022, 55, 7879−7892

https://pubs.acs.org/10.1021/acs.macromol.2c01216

Notes

The authors declare no competing financial interest.

■ ACKNOWLEDGMENTS

This study was supported financially by the Ministry of Science and Technology, Taiwan, under contracts MOST 111-2223-E-110-004 and 108-2221-E-110-014-MY3. The authors thank the staff at the National Sun Yat-sen University for their assistance with the TEM (ID: EM022600) experiments. The authors also thank Prof. Jyh-Tsung Lee at the National Sun Yat-sen University for their assistance with the EIS characterization.

■ REFERENCES

(1) Konnola, R.; Anirudhan, T. S. Efficient carbon dioxide capture by nitrogen and sulfur dual-doped mesoporous carbon spheres from polybenzoxazines synthesized by a simple strategy. *J. Environ. Chem. Eng.* **2020**, *8*, No. 103614.

(2) Shi, X.; Zhang, Z.; Wei, M.; Wang, X.; Wang, J.; Zhang, Y.; Wang, Y. Three-Dimensional Covalent Organic Framework Membranes: Synthesis by Oligomer Interfacial Ripening and Application in Precise Separations. *Macromolecules* **2022**, *55*, 3259−3266.

(3) Shi, W.; Zhang, X.; Ji, Y.; Zhao, Z.; Li, W.; Xudong Jia, X. Sustainable Preparation of Bio-Based Polybenzoxazine Resins from Amino Acid and Their Application in CO_2 Adsorption. *ACS Sustainable Chem. Eng.* **2019**, *7*, 17313−17324.

(4) Zhang, Y.; Zhang, L.; Zhang, X.; Yang, D.; Du, C.; Wan, L.; Au, C.; Chen, J.; Xie, M. Pyridine-based hypercrosslinked polymers as support materials for palladium photocatalysts and their application in Suzuki−Miyaura coupling reactions. *New J. Chem.* **2020**, *44*, 15202−15208.

(5) Ru, C.; Zhou, T.; Zhang, J.; Wu, X.; Sun, P.; Chen, P.; Zhou, L.; Zhao, H.; Wu, J.; Pan, X. Introducing Secondary Acceptors into Conjugated Polymers to Improve Photocatalytic Hydrogen Evolution. *Macromolecules* **2021**, *54*, 8839−8848.

(6) Abid, A.; Razzaque, S.; Hussain, I.; Tan, B. Eco-Friendly Phosphorus and Nitrogen-Rich Inorganic−Organic Hybrid Hypercross-linked Porous Polymers via a Low-Cost Strategy. *Macromolecules* **2021**, *54*, 5848−5855.

(7) Das, S.; Heasman, P.; Ben, T.; Qiu, S. Porous organic materials: strategic design and structure−function correlation. *Chem. Rev.* **2017**, *117*, 1515−1563.

(8) Tiwari, I.; Sharma, P.; Nebhani, L. Polybenzoxazine- an enticing precursor for engineering heteroatom-doped porous carbon materials with applications beyond energy, environment and catalysis. *Mater. Today Chem.* **2022**, *23*, No. 100734.

(9) Yang, S. J.; Ding, X.; Han, B. H. Conjugated microporous polymers with extended p-structures for organic vapor adsorption. *Macromolecules* **2018**, *51*, 947−953.

(10) Zhang, P.; Yin, Y.; Wang, Z.; Yu, C.; Zhu, Y.; Yan, D.; Liu, W.; Mai, Y. Porphyrin-Based Conjugated Microporous Polymer Tubes: Template-Free Synthesis and A Photocatalyst for Visible-Light-Driven Thiocyanation of Anilines. *Macromolecules* **2021**, *54*, 3543−3553.

(11) Hong, L.; Ju, S.; Liu, X.; Zhuang, Q.; Zhan, G.; Yu, X. Highly selective CO_2 uptake in novel fishnet-like polybenzoxazine-based porous carbon. *Energy Fuels* **2019**, *33*, 11454−11464.

(12) Zhang, T.; Xing, G.; Chen, W.; Chen, L. Porous organic polymers: a promising platform for efficient photocatalysis. *Mater. Chem. Front.* **2020**, *4*, 332−353.

(13) Yuan, Y.; Zhu, G. Porous aromatic frameworks as a platform for multifunctional applications. *ACS Cent. Sci.* **2019**, *5*, 409−418.

(14) Wu, J.-Y.; Mohamed, M. G.; Kuo, S. W. Directly synthesized nitrogen-doped microporous carbons from polybenzoxazine resins for carbon dioxide capture. *Polym. Chem.* **2017**, *8*, 5481−5489.

(15) Liang, H. P.; Acharjya, A.; Anito, D. A.; Vogl, S.; Wang, T. X.; Thomas, A.; Han, B. H. Rhenium-metalated polypyridine-based porous polycarbazoles for visible-light CO_2 photoreduction. *ACS Catal.* **2019**, *9*, 3959−3968.

(16) Wan, L.; Wang, J.; Feng, C.; Sun, Y.; Li, K. Synthesis of polybenzoxazine based nitrogen-rich porous carbons for carbon dioxide capture. *Nanoscale* **2015**, *7*, 6534−6544.

(17) Mohamed, M. G.; EL-Mahdy, A. F. M.; Kotp, M. G.; Kuo, S. W. Advances in porous organic polymers: syntheses, structures, and diverse applications. *Mater. Adv.* **2022**, *3*, 707−733.

(18) Manmuanpom, N.; Thubsuang, U.; Dubas, S. T.; Wongkasemjit, S.; Chaisuwan, T. Enhanced CO_2 capturing over ultra-microporous carbon with nitrogen-active species prepared using one-step carbonization of polybenzoxazine for a sustainable environment. *J. Environ. Manage.* **2018**, *223*, 779−786.

(19) Du, J.; Chen, A.; Liu, L.; Li, B.; Zhang, Y. N-doped hollow mesoporous carbon spheres prepared by polybenzoxazines precursor for energy storage. *Carbon* **2020**, *160*, 265−272.

(20) Guo, Z.; Lu, X.; Xin, Z. N, S, O co-doped porous carbons derived from bio-based polybenzoxazine for efficient CO_2 capture. *Colloids Surf., A* **2022**, *646*, No. 128845.

(21) Samy, M. M.; Mekhemer, I. M. A.; Mohamed, M. G.; Elsayed, M. H.; Lin, K.-H.; Chen, Y.-K.; Wu, T.-L.; Chou, H.-H.; Kuo, S.-W. Conjugated Microporous Polymers Incorporating Thiazolo[5,4-*d*]-thiazole Moieties for Sunlight-Driven Hydrogen Production From Water. *Chem. Eng. J.* **2022**, *446*, No. 137158.

(22) Côté, A. P.; Benin, A. I.; Ockwig, N. W.; O'Keeffe, M.; Matzger, A. I.; Yaghi, O. M. Porous, Crystalline, Covalent Organic Frameworks. *Science* **2005**, *310*, 1166−1170.

(23) Sprick, R. S.; Jiang, J. X.; Bonillo, B.; Ren, S.; Ratvijitvech, T.; Guiglion, P.; Zwijnenburg, M. A.; Adams, D. J.; Cooper, A. I. Tunable Organic Photocatalysts for Visible-Light-Driven Hydrogen Evolution. *J. Am. Chem. Soc.* **2015**, *137*, 3265−3270.

(24) Mohamed, M. G.; Elsayed, M. H.; Elewa, A. M.; El-Mahdy, A. F. M.; Yang, C. H.; Mohammed, A. A. K.; Chou, H. H.; Kuo, S. W. Pyrene-Containing Conjugated Organic Microporous Polymers for Photocatalytic Hydrogen Evolution from Water. *Catal. Sci. Technol.* **2021**, *11*, 2229−2241.

(25) Yuan, D.; Lu, W.; Zhao, D.; Zhou, H. C. Highly Stable Porous Polymer Networks with Exceptionally High Gas-Uptake Capacities. *Adv. Mater.* **2011**, *23*, 3723−3725.

(26) Chen, D.; Fu, Y.; Yu, W.; Yu, G.; Pan, C. Versatile Adamantane-based porous polymers with enhanced microporosity for efficient CO_2 capture and iodine removal. *Chem. Eng. J.* **2018**, *334*, 900−906.

(27) Sun, L.; Zou, Y.; Liang, Z.; Yu, J.; Xu, R. A one-pot synthetic strategy via tandem Suzuki−Heck reactions for the construction of luminescent microporous organic polymers. *Polym. Chem.* **2014**, *5*, 471−478.

(28) Lan, Y.; Yang, C.; Zhang, Y.; An, W.; Xue, H.; Ding, S.; Zhou, P.; Wang, W. Pyrrolidine-based chiral porous polymers for heterogeneous organocatalysis in water. *Polym. Chem.* **2019**, *10*, 3298−3305.

(29) Sun, L.; Liang, Z.; Yu, J.; Xu, R. Luminescent microporous organic polymers containing the 1,3,5-tri (4-ethenylphenyl) benzene unit constructed by Heck coupling reaction. *Polym. Chem.* **2013**, *4*, 1932−1938.

(30) Zhang, G.; Ou, W.; Wang, J.; Xu, Y.; Xu, D.; Sun, T.; Xiao, S.; Wang, M.; Li, H.; Chen, W.; Su, C. Stable, carrier separation tailorable conjugated microporous polymers as a platform for highly efficient photocatalytic H_2 evolution. *Appl. Catal., B* **2019**, *245*, 114−121.

(31) Wang, S.; Liu, Y.; Ye, Y.; Meng, X.; Du, J.; Song, X.; Liang, Z. Ultrahigh volatile iodine capture by conjugated microporous polymer based on N,N,N',N'-tetraphenyl-1,4-phenylenediamine. *Polym. Chem.* **2019**, *10*, 2608−2615.

(32) Samy, M. M.; Mohamed, M. G.; Mansoure, T. H.; Meng, T. S.; Khan, M. A. R.; Liaw, C. C.; Kuo, S. W. Solid state chemical transformations through ring-opening polymerization of ferrocene-based conjugated microporous polymers in host−guest complexes with benzoxazine-linked cyclodextrin. *J. Taiwan Inst. Chem. Eng.* **2022**, *132*, No. 104110.

(33) Wei, Z.; Chen, Q.; Liu, H. Hydroxyl modified hypercrosslinked polymers: targeting high efficient adsorption separation towards aniline. *New J. Chem.* **2021**, *45*, 11607−11617.
(34) Wei, Z.; Wang, D.; Liu, Y.; Guo, X.; Zhu, Y.; Meng, Z.; Yu, Z.-Q.; Wong, W.-Y. Ferrocene-based hyperbranched polymers: a synthetic strategy for shape control and applications as electroactive materials and precursor-derived magnetic ceramics. *J. Mater. Chem. C* **2020**, *8*, 10774−10780.
(35) Mohamed, M. G.; Chaganti, S. V.; Li, M. S.; Samy, M. M.; Sharma, S. U.; Lee, J. T.; Elsayed, M. H.; Chou, H. H.; Kuo, S. W. Ultrastable Porous Organic Polymers Containing Thianthrene and Pyrene Units as Organic Electrode Materials for Supercapacitors. *ACS Appl. Energy Mater.* **2022**, *5*, 6442−6452.
(36) Mohamed, M. G.; Liu, N.-Y.; EL-Mahdy, A. F. M.; Kuo, S.-W. Ultrastable luminescent hybrid microporous polymers based on polyhedral oligomeric silsesquioxane for CO_2 uptake and metal ion sensing. *Microporous Mesoporous Mater.* **2021**, *311*, No. 110695.
(37) Gu, C.; Huang, N.; Chen, Y.; Qin, L.; Xu, H.; Zhang, S.; Li, F.; Ma, Y.; Jiang, D. π-conjugated microporous polymer films: designed synthesis, conducting properties, and photoenergy conversions. *Angew. Chem.* **2015**, *127*, 13798−13802.
(38) Mohamed, M. G.; Atayde, E. C., Jr; Matsagar, B. M.; Na, J.; Yamauchi, Y.; Wu, K. C.-W.; Kuo, S.-W. Construction hierarchically mesoporous/microporous materials based on block copolymer and covalent organic framework. *J. Taiwan Inst. Chem. Eng.* **2020**, *112*, 180−192.
(39) Mohamed, M. G.; Lee, C.-C.; EL-Mahdy, A. F. M.; Lüder, J.; Yu, M.-H.; Li, Z.; Zhu, Z.; Chueh, C.-C.; Kuo, S.-W. Exploitation of two-dimensional conjugated covalent organic frameworks based on tetraphenylethylene with bicarbazole and pyrene units and applications in perovskite solar cells. *J. Mater. Chem. A* **2020**, *8*, 11448−11459.
(40) Xue, D.; Zhu, D.; Xiong, W.; Cao, T.; Wang, Z.; Lv, Y.; Li, L.; Liu, M.; Gan, L. Template-free, self-doped approach to porous carbon spheres with high N/O contents for high-performance supercapacitors. *ACS Sustainable Chem. Eng.* **2019**, *7*, 7024−7034.
(41) Stewart, D.; Antypov, D.; Dyer, M. S.; Pitcher, M. J.; Katsoulidis, A. P.; Chater, P. A.; Blanc, F.; Rosseinsky, M. J. Stable and Ordered Amide Frameworks Synthesised under Reversible Conditions which Facilitate Error Checking. *Nat. Commun.* **2017**, *8*, No. 1102.
(42) Waller, P. J.; Alfaraj, Y. S.; Diercks, C. S.; Jarenwattananon, N. N.; Yaghi, O. M. Conversion of Imine to Oxazole and Thiazole Linkages in Covalent Organic Frameworks. *J. Am. Chem. Soc.* **2018**, *140*, 9099−9103.
(43) Liu, H.; Chu, J.; Yin, Z.; Cai, X.; Zhuang, L.; Deng, H. Covalent Organic Frameworks Linked by Amine Bonding for Concerted Electrochemical Reduction of CO_2. *Chem* **2018**, *4*, 1696−1709.
(44) Haase, F.; Troschke, E.; Savasci, G.; Banerjee, T.; Duppel, V.; Dorfler, S.; Grundei, M. M. J.; Burow, A. M.; Ochsenfeld, C.; Kaskel, S.; Lotsch, B. V. Topochemical Conversion of an Imine- into A Thiazole-Linked Covalent Organic Framework Enabling Real Structure Analysis. *Nat. Commun.* **2018**, *9*, No. 2600.
(45) Waller, P. J.; Lyle, S. J.; Popp, T. O.; Diercks, C. S.; Reimer, J. A.; Yaghi, O. M. Chemical Conversion of Linkages in Covalent Organic Frameworks. *J. Am. Chem. Soc.* **2016**, *138*, 15519−15522.
(46) Zhao, C.; Lyu, H.; Ji, Z.; Zhu, C.; Yaghi, O. M. Ester-Linked Crystalline Covalent Organic Frameworks. *J. Am. Chem. Soc.* **2020**, *142*, 14450−14454.
(47) Haase, F.; Hirschle, P.; Freund, R.; Furukawa, S.; Ji, Z.; Wuttke, S. Beyond Frameworks: Structuring Reticular Materials Across Nano-, Meso-, and Bulk Regimes. *Angew. Chem., Int. Ed.* **2020**, *59*, 22350−22370.
(48) Lyle, S. J.; Popp, T. O. S.; Waller, P. J.; Pei, X.; Reimer, J. A.; Yaghi, O. M. Multistep Solid-State Organic Synthesis of Carbamate-Linked Covalent Organic Frameworks. *J. Am. Chem. Soc.* **2019**, *141*, 11253−11258.
(49) Kim, H.-D.; Ishida, H. A Study on Hydrogen-Bonded Network Structure of Polybenzoxazines. *J. Phys. Chem. A* **2002**, *106*, 3271−3280.
(50) Zhang, S.; Ran, Q.; Fu, Q.; Gu, Y. Thermal responsiveness of hydrogen bonding and dielectric property of polybenzoxazines with different Mannich bridge structures. *Polymer* **2019**, *175*, 302−309.
(51) Lyu, Y.; Ishida, H. Natural-Sourced Benzoxazine Resins, Homopolymers, Blends and Composites: A Review of Their Synthesis, Manufacturing and Applications. *Prog. Polym. Sci.* **2019**, *99*, No. 101168.
(52) Mohamed, M. G.; Kuo, S. W. Functional Silica and Carbon Nanocomposites Based on Polybenzoxazines. *Macromol. Chem. Phys.* **2019**, *220*, No. 1800306.
(53) Mohamed, M. G.; Li, C. J.; Khan, M. A. R.; Liaw, C. C.; Zhang, K.; Kuo, S. W. Formaldehyde-Free Synthesis of Fully Bio-Based Multifunctional Bisbenzoxazine Resins from Natural Renewable Starting Materials. *Macromolecules* **2022**, *55*, 3106−3115.
(54) Mohamed, M. G.; Kuo, S. W. Crown Ether-Functionalized Polybenzoxazine for Metal Ion Adsorption. *Macromolecules* **2020**, *53*, 2420−2429.
(55) Shen, X.; Cao, L.; Liu, Y.; Dai, J.; Liu, X.; Zhu, J.; Du, S. How Does the Hydrogen Bonding Interaction Influence the Properties of Polybenzoxazine? An Experimental Study Combined with Computer Simulation. *Macromolecules* **2018**, *51*, 4782−4799.
(56) Xu, S.; He, J.; Jin, S.; Tan, B. Heteroatom-Rich Porous Organic Polymers Constructed by Benzoxazine Linkage with High Carbon Dioxide Adsorption Affinity. *J. Colloid Interface Sci.* **2018**, *509*, 457−462.
(57) Abuzeid, H. R.; El-Mahdy, A. F. M.; Ahmed, M. M. M.; Kuo, S. W. Triazine-Functionalized Covalent Benzoxazine Framework for Direct Synthesis of N-Doped Microporous Carbon. *Polym. Chem.* **2019**, *10*, 6010−6020.
(58) Sun, X.; Li, J.; Wang, W.; Ma, Q. Constructing Benzoxazine-Containing Porous Organic Polymers for Carbon Dioxide and Hydrogen Sorption. *Eur. Polym. J.* **2018**, *107*, 89−95.
(59) Mohamed, M. G.; Chen, T. C.; Kuo, S. W. Solid-State Chemical Transformations to Enhance Gas Capture in Benzoxazine-Linked Conjugated Microporous Polymers. *Macromolecules* **2021**, *54*, 5866−5877.
(60) Li, J.; Yim, D.; Jang, W. D.; Yoon, J. A Recent progress in the design and applications of fluorescence probes containing crown ethers. *Chem. Soc. Rev.* **2017**, *46*, 2437−2458.
(61) Huang, D.; Zhang, Q.; Deng, Y.; Luo, Z.; Li, B.; Shen, X.; Qi, Z.; Dong, S.; Ge, Y.; Chen, W. Polymeric crown ethers: LCST behavior in water and stimuli-responsiveness. *Polym. Chem.* **2018**, *9*, 2574−2579.
(62) Patel, H. A.; Selberg, J.; Salah, D.; Chen, H.; Liao, Y.; Mohan Nalluri, S. K.; Farha, O. K.; Snurr, R. Q.; Rolandi, M.; Stoddart, J. F. Proton Conduction in Tröger's Base-Linked Poly(crown ether)s. *ACS Appl. Mater. Interfaces* **2018**, *10*, 25303−25310.
(63) Marczenko, K. M.; Mercier, H. P. A.; Schrobilgen, G. J. A Stable Crown Ether Complex with a Noble-Gas Compound. *Angew. Chem., Int. Ed.* **2018**, *57*, 12448−12452.
(64) Kazemabad, M.; Verliefde, A.; Cornelissen, E. R.; D'Haese, A. Crown ether containing polyelectrolyte multilayer membranes for lithium recovery. *J. Membr. Sci.* **2020**, *595*, No. 117432.
(65) Chen, W.; Chen, P.; Zhang, G.; Xing, G.; Feng, Y.; Yang, Y. W.; Chen, L. Macrocycle-derived hierarchical porous organic polymers: synthesis and applications. *Chem. Soc. Rev.* **2021**, *50*, 11684−11714.
(66) Kong, H. Y.; Wang, T. X.; Tao, Y.; Ding, X.; Han, B. H. Crown ether-based hypercrosslinked porous polymers for gold adsorption. *Sep. Purif. Technol.* **2022**, *290*, No. 120805.
(67) An, S.; Xu, Q.; Ni, Z.; Hu, J.; Peng, C.; Zhai, L.; Guo, Y.; Liu, H. Construction of covalent organic frameworks with crown ether struts. *Angew. Chem., Int. Ed.* **2021**, *60*, 9959−9963.
(68) Xu, T.; He, Y.; Qin, Y.; Zhao, C.; Peng, C.; Hu, J.; Liu, H. Facile preparation of porous organic copolymer based on triptycene and crown ether for efficient organic dye adsorption. *RSC Adv.* **2018**, *8*, 4963−4968.

https://doi.org/10.1021/acs.macromol.2c01216
Macromolecules 2022, 55, 7879−7892

(69) Zhang, X.; Mohamed, M. G.; Xin, Z.; Kuo, S. W. A tetraphenylethylene-functionalized benzoxazine and copper(II) acetylacetonate form a high-performance polybenzoxazine. *Polymer* **2020**, *201*, No. 122552.
(70) Shi, W.; Liu, Q.; Zhang, J.; Zhou, X.; Yang, C.; Zhang, K.; Xie, Z. Tetraphenylethene-decorated functional polybenzoxazines: post-polymerization synthesis via benzoxazine−isocyanide chemistry and application in probing and catalyst fields. *Polym. Chem.* **2019**, *10*, 1130−1139.
(71) Su, Y.; Shi, W.; Chen, X.; Zhao, S.; Hui, Y.; Xie, Z. An aggregation-induced emission enhancement fluorescent benzoxazine-derived macromolecule: catalyst-free synthesis and its preliminary application for the determination of aqueous picric acid. *RSC Adv.* **2016**, *6*, 41340−41347.
(72) Luo, Z.-W.; Tao, L.; Zhong, C.; Li, Z.; Lan, K.; Feng, Y.; Wang, P.; Xie, H. High-Efficiency Circularly Polarized Luminescence from Chiral Luminescent Liquid Crystalline Polymers with Aggregation-Induced Emission Properties. *Macromolecules* **2020**, *53*, 9758−9768.
(73) Wan, L.; Wang, J.; Sun, Y.; Feng, C.; Li, K. Polybenzoxazine-Based Nitrogen-Containing Porous Carbons for High-Performance Supercapacitor Electrodes and Carbon Dioxide Capture. *RSC Adv.* **2015**, *5*, 5331−5342.
(74) Wan, L.; Wang, J.; Feng, C.; Sun, Y.; Li, K. Synthesis of Polybenzoxazine Based Nitrogen-Rich Porous Carbons for Carbon Dioxide Capture. *Nanoscale* **2015**, *7*, 6534−6544.
(75) Mohamed, M. G.; Samy, M. M.; Mansoure, T. H.; Li, C. J.; Li, W. C.; Chen, J. H.; Zhang, K.; Kuo, S. W. Microporous Carbon and Carbon/Metal Composite Materials Derived from Bio-Benzoxazine-Linked Precursor for CO_2 Capture and Energy Storage Applications. *Int. J. Mol. Sci.* **2022**, *23*, No. 347.
(76) Liu, C.; Shen, D.; Sebastian, R. M.; Marquet, J.; Schönfeld, R. Mechanistic Studies on Ring-Opening Polymerization of Benzoxazines: A Mechanistically Based Catalyst Design. *Macromolecules* **2011**, *44*, 4616−4622.
(77) Mohamed, M. G.; Su, W.-C.; Lin, Y.-C.; Wang, C.-F.; Chen, J.-K.; Jeong, K.-U.; Kuo, S.-W. Azopyridine-functionalized benzoxazine with $Zn(ClO_4)_2$ form high-performance polybenzoxazine stabilized through metal-ligand coordination. *RSC Adv.* **2014**, *4*, 50373−50385.
(78) An, S.; Lu, C.; Xu, Q.; Lian, C.; Peng, C.; Hu, J.; Zhuang, X.; Liu, H. Constructing Catalytic Crown Ether-Based Covalent Organic Frameworks for Electroreduction of CO_2. *ACS Energy Lett.* **2021**, *6*, 3496−3502.
(79) Yuan, L.; Zhu, J.; Wu, S.; Chi, C. Enhanced emission by stacking of crown ether side chains in a 2D covalent organic framework. *Chem. Commun.* **2022**, *58*, 1302−1305.
(80) Shen, J. C.; Jiang, W. L.; Guo, W. D.; Qi, Q. Y.; Ma, D. L.; Lou, X.; Shen, M.; Hu, B.; Yang, H. B.; Zhao, X. A rings-in-pores net: crown ether-based covalent organic frameworks for phase-transfer catalysis. *Chem. Commun.* **2020**, *56*, 595−598.
(81) Konnola, R.; Anirudhan, T. S. Efficient carbon dioxide capture by nitrogen and sulfur dual-doped mesoporous carbon spheres from polybenzoxazines synthesized by a simple strategy. *J. Environ. Chem. Eng.* **2020**, *8*, 103614−103624.
(82) Huang, L.; Liu, J.; Lin, H. Thermally stable, homogeneous blends of cross-linked poly(ethylene oxide) and crown ethers with enhanced CO_2 permeability. *J. Membr. Sci.* **2020**, *610*, No. 118253.
(83) Weng, Z.; Su, Y.; Wang, D. W.; Li, F.; Du, J.; Cheng, H. M. Graphene−cellulose paper flexible supercapacitors. *Adv. Energy Mater.* **2011**, *1*, 917−922.
(84) Xu, R.; Guo, F.; Cui, X.; Zhang, L.; Wang, K.; Wei, J. High performance carbon nanotube-based fiber-shaped supercapacitors using redox additives of polypyrrole and hydroquinone. *J. Mater. Chem. A* **2015**, *3*, 22353−22360.

Recommended by ACS

Highly Nitrogen-Rich Microporous Polyaminals Using *N*,*N*-Dimethylformamide and Formamide as the Starting Monomers for CO_2 Adsorption and Separation

Gen Li, Zhonggang Wang, *et al.*
JANUARY 22, 2020
THE JOURNAL OF PHYSICAL CHEMISTRY C
READ

Triptycene-Based and Schiff-Base-Linked Porous Networks: Efficient Gas Uptake, High CO_2/N_2 Selectivity, and Excellent Antiproliferative Activity

Akhtar Alam, Neeladri Das, *et al.*
FEBRUARY 21, 2020
ACS OMEGA
READ

Solid-State Chemical Transformations to Enhance Gas Capture in Benzoxazine-Linked Conjugated Microporous Polymers

Mohamed Gamal Mohamed, Shiao-Wei Kuo, *et al.*
MAY 21, 2021
MACROMOLECULES
READ

One-Step Synthesis of an Ionic Covalent Organic Polymer for CO_2 Capture

Syed Ibrahim Gnani Peer Mohamed, Siamak Nejati, *et al.*
OCTOBER 11, 2022
ACS APPLIED POLYMER MATERIALS
READ

Get More Suggestions >

https://doi.org/10.1021/acs.macromol.2c01216
Macromolecules 2022, 55, 7879−7892